Research Square

Preprints are preliminary reports that have not undergone peer review.
They should not be considered conclusive, used to inform clinical practice,
or referenced by the media as validated information.

Polymerization of Porphyrins by Indenyl Coupling

David Ecija

david.ecija@imdea.org

IMDEA Nanoscience https://orcid.org/0000-0002-8661-8295

Alba Garcia-Frutos

IMDEA Nanoscience

Ana Barragán

IMDEA Nanoscience, C/Faraday 9, Campus de Cantoblanco https://orcid.org/0000-0003-2570-5018

Ana Monteiro

Centro Singular de Investigación en Química Biolóxica e Materiais Moleculares (CIQUS)
https://orcid.org/0000-0003-2528-943X

Tianchen Qin

IMDEA Nanoscience

Jesús Bello-García

Centro Singular de Investigación en Química Biolóxica e Materiais Moleculares (CIQUS)
https://orcid.org/0000-0002-6767-5913

Rubén Canales

Instituto de Ciencia de Materiales de Madrid (ICMM), CSIC

Alberto Martínez-Bajo

IMDEA Nanoscience

Koen Lauwaet

IMDEA Nanoscience https://orcid.org/0000-0003-1024-6779

Pablo Merino

Instituto de Ciencia de Materiales de Madrid (ICMM), CSIC

José Ignacio Urgel

IMDEA Nanoscience https://orcid.org/0000-0001-7608-2979

Dolores Pérez

CIQUS, Universidade de Santiago de Compostela https://orcid.org/0000-0003-0877-5938

Borja Cirera

Instituto de Ciencia de Materiales de Madrid (ICMM), CSIC

Jose Martinez

ICMM-CSIC https://orcid.org/0000-0002-2086-8603

Aurelio Gallardo

IMDEA Nanoscience https://orcid.org/0000-0001-6544-7637

Diego Peña
Universidade de Santiago de Compostela https://orcid.org/0000-0003-3814-589X

Article

Keywords:

Posted Date: November 10th, 2026

DOI: https://doi.org/10.21203/rs.3.rs-11614027/v1

License: This work is licensed under a Creative Commons Attribution 4.0 International License.
Read Full License

Additional Declarations: There is **NO** Competing Interest.

Polymerization of Porphyrins by Indenyl Coupling

Alba García-Frutos[1,†], Ana Barragán[1,3,†,*], Ana R. Monteiro[2,†,*], Tianchen Qin[1], Jesús Bello-García[2], Rubén Canales[4], Alberto Martínez-Bajo[1], Koen Lauwaet[1], Pablo Merino[3,4], José I. Urgel[1,3], Dolores Pérez[2], Borja Cirera[3,4], José I. Martínez[3,4], Aurelio Gallardo[1], Diego Peña[2,5*] and David Écija[1,3*]

[1]IMDEA Nanoscience, Campus de Cantoblanco, 28049 Madrid, Spain
[2]Centro Singular de Investigación en Química Biolóxica e Materiais Moleculares (CiQUS) and Departamento de Química Orgánica, Universidade de Santiago de Compostela, 15782 Santiago de Compostela, Spain
[3]Unidad de Nanomateriales Avanzados, IMDEA Nanoscience, Unidad asociada al CSIC por el ICMM, 28049 Madrid, Spain
[4]Instituto de Ciencia de Materiales de Madrid (ICMM), CSIC, 28049 Madrid, Spain
[5]Oportunius, Galician Innovation Agency (GAIN), Santiago de Compostela, 15702, Spain.

* Address correspondence to these authors.

† These authors contributed equally.

Abstract

Porphyrin polymers merge the photophysical, electrochemical, sensory and catalytic properties of porphyrins with the processability and robustness of polymeric materials, offering versatile and synergetic platforms for optoelectronics and catalysis. Here we report an on-surface strategy for the atomically precise polymerization of porphyrins via regioselective indenyl coupling. Deposition of an indenyl-functionalized porphyrin on Au(111) and sequential annealing drives a stepwise transformation: cyclodehydrogenation at 100 °C planarizes the precursor into π-extended porphyrins, while annealing above 125 °C triggers carbon–carbon homocoupling through five-membered moieties, forming short oligomers. Heating to 150 °C promotes chain growth into one-dimensional polymers with a 1.1 eV bandgap and extended π delocalization, alongside a minor fraction of cyclic trimers featuring a 1.1 eV HOMO–LUMO gap with both local and global aromaticity. The methodology also proceeds for Co-metallated precursors, confirming that indenyl coupling is also compatible for metalloporphyrins, establishing a general route to design π-extended porphyrin polymers.

Porphyrins constitute a versatile family of macrocyclic molecules that play a central role in both natural processes and technological applications. Their electronic structure can be precisely modified, making them valuable across disciplines from renewable energy research to medical diagnostics. The unique combination of light-absorbing capabilities, metal-binding characteristics, and molecular recognition properties positions these compounds as candidates for catalyst development and chemical sensing platforms.[1] Biologically, porphyrin-based structures are indispensable since the heme group enables oxygen delivery and electron transfer in numerous proteins,[2,3] while chlorophyll molecules capture solar energy to power photosynthesis in plants.[3,4] On the technological front, their capacity to absorb and emit visible light has sparked interest in optoelectronic devices, including solar cells, organic electronic materials, and LED technologies.[5,6] Their discriminating binding behavior also makes them attractive for sensor applications targeting specific gases, metal ions, and biological markers.[7] Beyond sensing, porphyrins serve as biomimetic catalysts that replicate enzymatic functions in chemical transformations.[8,9] Recent investigations further highlight their potential contributions to next-generation energy storage technologies, encompassing advanced battery designs and fuel cell systems.[10]

Building on this versatile foundation, porphyrin polymers represent a fascinating class of macromolecular materials that bridge the gap between biological systems and synthetic chemistry. The resulting materials combine the unique properties of porphyrins with the processability of polymers, creating opportunities for applications ranging from organic electronics to catalysis and photodynamic therapy.[11-14] To fully realize this potential, the exploration of novel synthetic strategies to access unique polymeric architectures is essential.

Over the past two decades, the development of on-surface covalent synthesis has established a new paradigm in chemistry. Conducted under ultra-high vacuum (UHV), this strategy uses surfaces to drive covalent reactions[15-22] and enables direct, atomic-scale imaging of the products.[23] It has proven powerful for synthesizing structures that are challenging for solution-phase chemistry, yielding a growing array of unique materials including nanographenes, one-dimensional wires, nanoribbons, and two-dimensional covalent organic frameworks,[15-22] although typically relying on Ullmann coupling,[24-26] which involves undesirable halogen byproducts on the surface.

In particular, recognizing the significance of porphyrins, the surface science community, assisted by scanning probe microscopy, has focused on studies of their adsorption, conformation, self-assembly, metalation of their inner cavity and on-surface reactivity.[27-40] Despite this extensive investigation into their surface properties, the polymerization chemistry for creating porphyrin polymers remains underdeveloped and limited to very few on-surface chemical reactions.[32,35,37,38,41-48]

In this manuscript, we introduce a pioneering on-surface synthesis protocol to homocouple porphine derivatives into covalent zero-dimensional (0D) cyclic trimers and one-dimensional (1D) linear polymers via the recently established regioselective indenyl coupling (see Figure 1a)[49]. To this end, a porphine species (**1**) was rationally designed and synthesized incorporating a dicyclopentaanthracene (DCPA) moiety, an acene derivative that comprises two terminal indane moieties.[50] Upon deposition on an Au(111) substrate held at room temperature and subsequent annealing at 100 °C, this precursor undergoes cyclodehydrogenation forming individual and planar species **2**. Further annealing above 125 °C activates the homocoupling

through indenyl coupling between the two five-membered ring terminal moieties, with the resulting polymers (**3**) growing longer at higher annealing temperatures. The dominant products are 1D linear polymers with a bandgap of 1.1 eV and extended π delocalization. Minor cyclic covalent trimers (**4**) are also detected, featuring a highest occupied molecular orbital-lowest unoccupied molecular orbital (HOMO–LUMO) gap of 1.1 eV. According to anisotropy of the induced current density (AICD) analysis, these trimers display global aromaticity[51] along the periphery (78π) and local aromaticity in the inner macrocyclic rings (18π), also confirmed by negative nucleus-independent chemical shift (NICS) values. The same reaction pathway is preserved for a Co-metallated precursor (**5**), illustrating universality of the coupling reaction for both free-base and metallated porphyrin precursors.

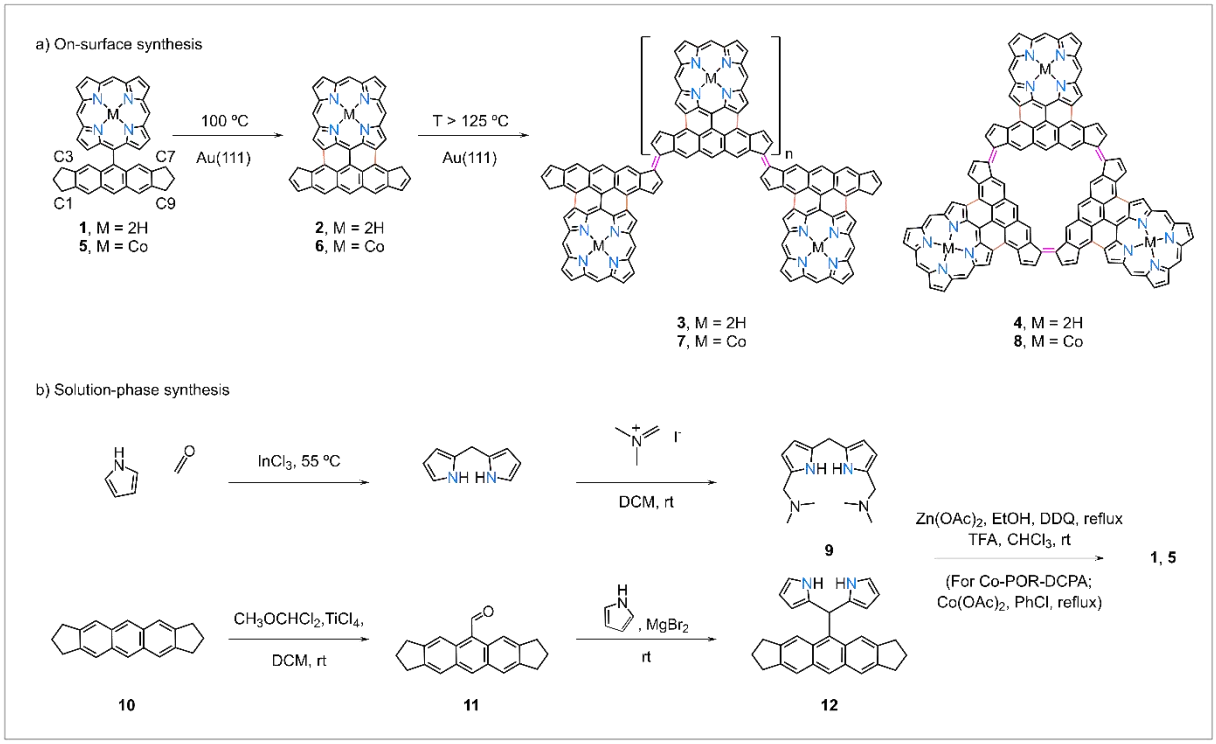


Figure 1 | On-surface synthesis of linear (3, 7) and cyclic (4, 8) porphyrin architectures via indenyl coupling and solution-phase synthesis of precursors 1 and 5. a. Deposition of free-base precursor **1** (M = 2H) or Co-metallated precursor **5** (M = Co) on Au(111) held at room temperature, followed by annealing at 100 °C induces cyclodehydrogenation (orange bonds), yielding species **2** (M = 2H) and **6** (M = Co), respectively. Further annealing above 125 °C promotes indenyl coupling (pink bonds) between neighbouring porphyrins, affording the linear polymers **3** (M = 2H) and **7** (M = Co) as the major products. Under these conditions, a minor fraction of cyclic porphyrin trimers **4** (M = 2H) and **8** (M = Co) is also formed. b. Solution-phase synthesis of the molecular precursors **1** (M = 2H) and **5** (M = Co).

Our work establishes a novel on-surface regioselective indenyl coupling route to fabricate and characterize unprecedented one-dimensional porphyrin polymers and cyclic trimers featuring complex aromaticity. The obtained porphyrinoids, with their engineered bandgaps and distinct electronic features, exemplify a significant breakthrough in the bottom-up construction of functional organic nanomaterials. Collectively, these findings set the stage for further advancements in the controlled fabrication of molecular architectures with bespoke electronic properties, holding clear implications for the development of next-generation systems in organic electronics, energy storage, sensing and catalysis.

RESULTS AND DISCUSSION

The molecular precursor was synthesized to steer the formation of a π-expanded porphyrin via intramolecular reactions,[21] which then could be polymerized thanks to the recently discovered indenyl coupling.[49,50] To this end, a free-base porphine precursor was functionalized with a DCPA moiety, which features two indane termini, as depicted in Figure 1.

In particular, we targeted 5-(1,2,3,7,8,9-hexahydrodicyclopenta[*b,i*]anthracen-5-yl)porphyrin (see Figure 1) in both the free-base form (**1**) and as a cobalt complex (**5**). A key intermediate in the synthesis illustrated in Figure 1 was 1,2,3,7,8,9-hexahydrodicyclopenta[*b,i*]anthracene-5-carbaldehyde (**11**), which was obtained *via* Rieche formylation of the corresponding anthracene **10**, itself prepared through a multistep aryne-chemistry strategy described in our recent work.[49,50] The aldehyde functionality of **11** enabled construction of the porphyrin core through established condensation of dipyrromethanes **9** and **12** (see Figures S1 – S10 in the SI), while the indenyl termini were incorporated to guide the following on-surface homocoupling at the metal interface. Complexation of the macrocycle with Co(II) was used to modulate the properties of the precursor and to investigate its effect on the electronic characteristics of the resulting porphyrin polymers. Full characterization of the precursors by nuclear magnetic resonance (NMR) spectroscopy and mass spectrometry (MS) confirmed their structure and purity, providing a robust starting point for subsequent on-surface polymerization studies.

The reaction products obtained after deposition of precursors **1** or **5** onto an atomically clean Au(111) surface and the subsequent post-annealing steps were discerned thanks to the complementary combination of scanning tunneling microscopy (STM) and non-contact atomic force microscopy (nc-AFM), assisted by density functional theory (DFT) calculations, as discussed below (cf. Figures 1-3 and Figures in the SI).

First, the sublimation of a submonolayer coverage of compound **1** onto Au(111) held at room temperature resulted in the adsorption of intact and non-planar species, as depicted in Figure S11. Upon annealing at 100 °C, the adsorbed precursors undergo intramolecular cyclodehydrogenation between the porphyrin and the DCPA framework, resulting in molecular planarization and the formation of individual π-extended porphyrins (**2**), as shown in Figure 2a. High-resolution STM and nc-AFM images, together with the corresponding simulated adsorbed geometry and nc-AFM image of **2** are presented in Figures 2b-f. The presence of two bright protrusions at the edges of the DCPA moiety in the nc-AFM images indicates that species **2** retains two additional hydrogen atoms. Attempts to remove these hydrogen atoms by tip-induced manipulation were unsuccessful. As observed in Figure 2f, the simulated nc-AFM image reproduces well the experimental one (cf. Figure 2d), supporting the proposed structure of **2**.

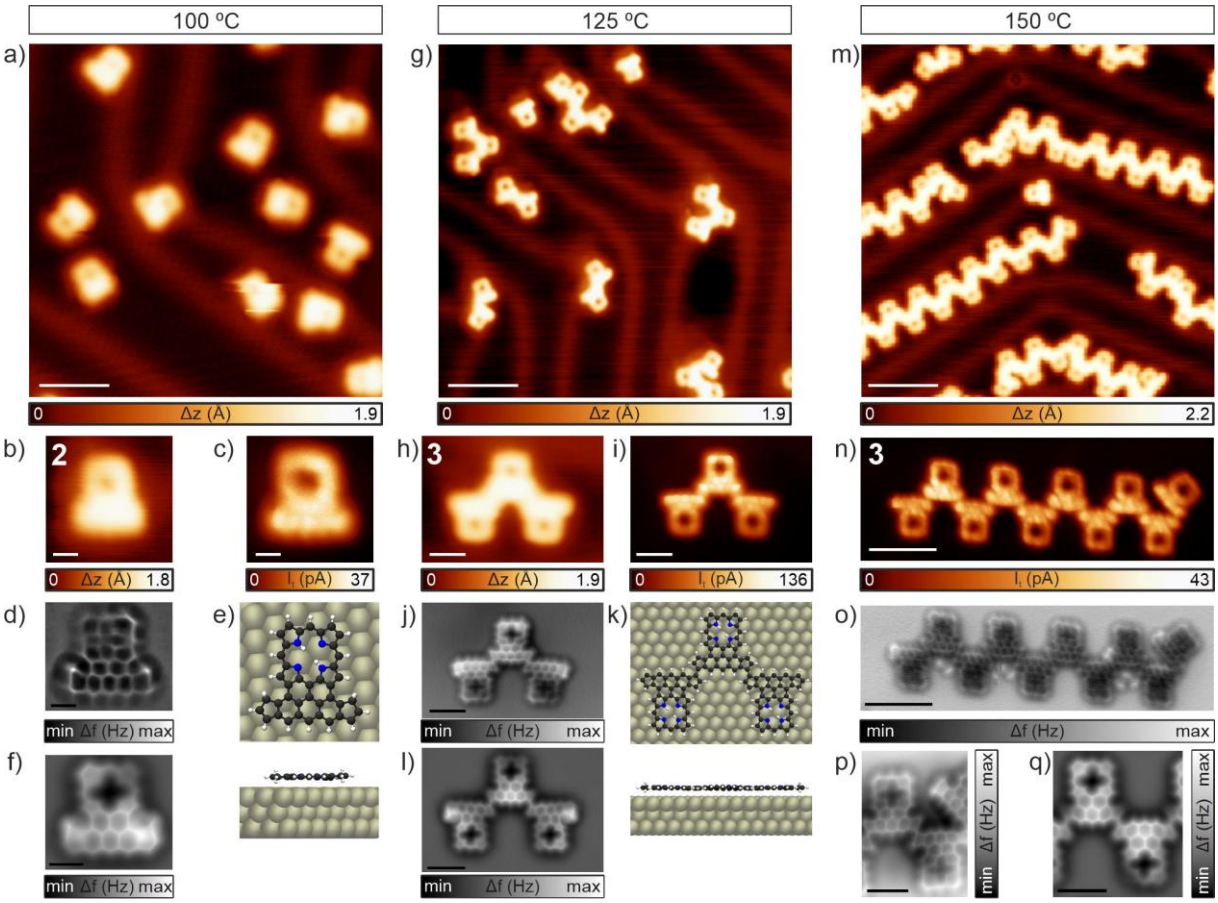


Figure 2 | On-surface synthesis of individual π-extended porphyrins 2 by cyclodehydrogenation, porphyrin oligomers, and 1D porphyrin polymers 3 by indenyl coupling. a. Overview STM image acquired after deposition of precursor **1** on Au(111) and annealing at 100 °C, showing individual planar species, **2.** (V_b = 0.50 V, I_t = 10 pA, scale bar = 2.2 nm). b, c. High-resolution constant-current and constant-height STM images of **2**, respectively. (V_b = 0.50 V, I_t = 50 pA, scale bar = 5.0 Å, and V_b = 5 mV, I_t = 50 pA, scale bar = 3.5 Å, respectively) d. Laplace-filtered nc-AFM image of **2**. (Z-offset: 160 pm above STM set point: 5 mV, 50 pA. Scale bar = 3.5 Å). e, f. Calculated adsorption geometry (top and side views) and corresponding simulated nc-AFM image (scale bar = 0.5 nm). g. Overview STM image acquired after deposition of precursor **1** on Au(111) and annealing at 125 °C, showing short oligomers of **3**, where n = 1. (V_b = 0.35 V, I_t = 50 pA, scale bar = 4.0 nm). h, i. High-resolution constant-current and constant-height STM images of **3** (n = 1), respectively. (V_b = 0.50 V, I_t = 50 pA, scale bar = 1.0 nm, and V_b = 5 mV, I_t = 50 pA, scale bar = 1.0 nm, respectively). j. Corresponding nc-AFM image. (Z-offset: 130 pm above STM set point: 5 mV, 50 pA. Scale bar = 1.0 nm). k, l. Calculated adsorption geometry (top and side views) and corresponding simulated nc-AFM image (scale bar = 0.5 nm) of **3** (n = 1), respectively. m. Overview STM image acquired after deposition of precursor **1** on Au(111) and annealing at 150 °C, showing long polymers of **3** (V_b = 1.00 V, I_t = 50 pA, scale bar = 4.0 nm). n, o. High-resolution constant-height STM image (V_b = 5 mV, I_t = 50 pA, scale bar = 2.2 nm) and nc-AFM image (Z-offset: 170 pm above STM set point: 5 mV, 50 pA. Scale bar = 2.2 nm) of decamer of polymer **3** (n = 8), respectively. p, q. Experimental (Z-offset: 150 pm above STM set point: 5 mV, 50 pA. Scale bar = 8.0 Å) and corresponding simulated (scale bar = 1 nm) nc-AFM images, respectively, of a zoomed-in region of the decamer of polymer **3**, illustrating the excellent agreement between experiment and theory.

Further annealing to 125 °C activates the regioselective indenyl coupling between neighbouring porphyrin derivatives, resulting in the formation of dimers and short linear oligomers of **3**, as shown in Figure 2g and Figure S12. Representative high-resolution STM and nc-AFM images of a selected free-base linear porphyrin-based trimer reveal the covalent connection of adjacent π-extended porphyrin units through their five membered rings. The observed bond-length alternation, supported by the corresponding nc-AFM simulations, is consistent with the proposed double carbon-carbon bonds via five-member moieties (cf. Figures 2h-l and bond-length alternation analysis in Figure S13). The calculated adsorption geometry of a trimer of **3** (cf. Figure 2k) matches well with the experimental findings revealing a flat adsorption on Au(111), and the agreement of experimental and simulated nc-AFM images is excellent (cf. Figures 2j and 2l). Importantly, resonance structures maximizing the number of Clar sextets

within the acene-derived framework may involve terminal radical centres (Supplementary Fig. S14 and discussion therein).[22,52,53] However, the additional protrusions observed at the oligomer termini in the nc-AFM images (cf. Figure 2j), together with the corresponding simulations, are consistent with hydrogen passivation of these positions. Such hydrogen termination provides a chemically plausible stabilization mechanism by saturating the terminal sites associated with the proposed open-shell resonance structures. Finally, the telegraphic signal of the current is observed in the STM signal when the tip is positioned over the cavities of the free-base porphyrins in both **2** and **3** (cf. Figure S15). We assign this behavior to porphyrin tautomerization[27,54,55] thereby confirming that the two inner hydrogen atoms remain intact after cyclodehydrogenation and polymerization.

The average polymer length increased by raising the annealing temperature to 150 °C (Figure 2m and Figure S16), affording longer free-base 1D staircase polymers (**3**) or cyclic porphyrin trimers (**4**). These polymers preferentially assemble along the FCC regions of the Au(111) herringbone reconstruction (cf. Figure 2m). Notably, the polymerization of porphyrins by indenyl coupling is also detected on Ag(111), yielding both linear and cyclic architectures, as illustrated in Figure S17. This demonstrates that the coupling reaction is not restricted to Au(111) and can also proceed on a different metal surface.

Subsequent post-annealing at 200 °C induced partial self-metallation of the porphyrin cavities by Au adatoms, as shown in Figure 3a-d, giving rise to metallation of most of the cavities at 250 °C (cf. Figure S18). Compared with the empty porphyrin cavities, Au-metallated centers appear as small protrusions in the constant-height STM images (cf. Figure 3b) and as bright cross-shaped features in the nc-AFM images (cf. Figure 3c).[56]

We next sought to extend the indenyl-coupling-based polymerization of porphyrin units to a broader range of metalloporphyrins. To this end, the same thermal protocol was applied to the Co-metallated precursor **5**, yielding analogous individual species **6** after annealing at 100 °C (Figure S19) and one-dimensional polymers **7** after annealing at 200 °C, without alteration of the metal centers (cf. Figure 3e-h), highlighting the generality of the indenyl coupling strategy for designing porphyrin polymers. In the Co-metallated polymers **7**, the Co centers appear as pronounced central protrusions in the constant-height STM images (cf. Figure 3f), whereas they appear as voids in the nc-AFM images (cf. Figure 3g).[57] For comparison, Co-metallated polymers could also be obtained by depositing Co atoms *in situ* onto the preformed free-base polymers (**3**) (Figure S20).

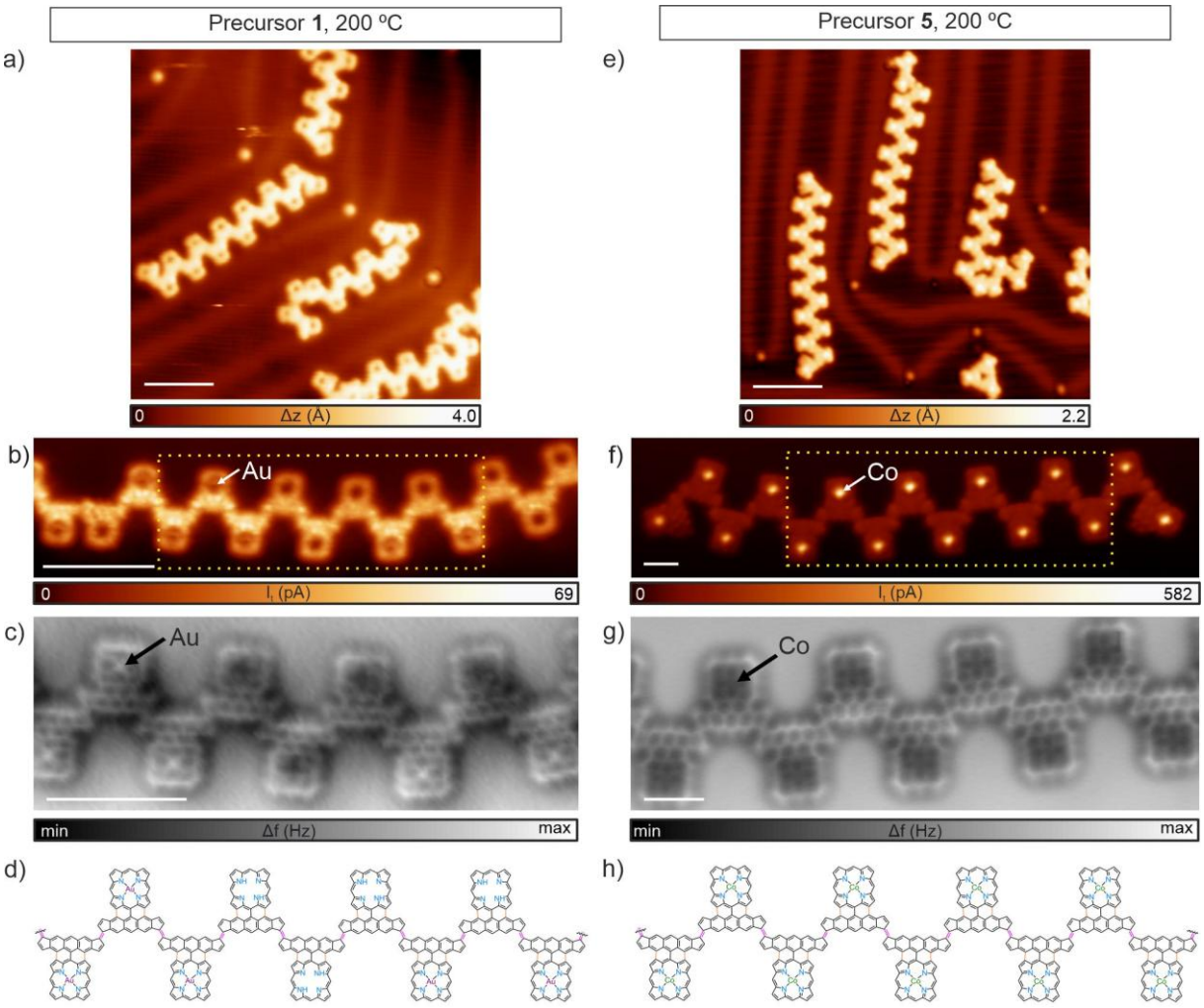


Figure 3 | Gold self-metallation of free-base porphyrin polymers and formation of Co-metallated porphyrin polymers, 7. a. Overview STM image after deposition of precursor **1** and post-annealing at 200 °C (V_b = 0.5 V, I_t = 50 pA, scale bar = 9.1 nm). b. High-resolution constant-height STM image of a long polymer after post-annealing at 200 °C (V_b = 5 mV, I_t = 50 pA, scale bar = 3.0 nm). c, d. nc-AFM image (Z-offset: 115 pm above STM set point: 5 mV, 50 pA. Scale bar = 3.0 nm) and corresponding chemical structure of the selected polymer region, highlighting the Au-metallated porphyrin centers. e. Overview STM image after deposition of Co-metallated precursor **5** on an Au(111) surface and subsequent post-annealing at 200 °C (V_b = 0.5 V, I_t = 40 pA, scale bar = 5.0 nm). f. High-resolution constant-height STM image of a long 1D Co-metallated polymer, **7** (V_b = 5 mV, I_t = 50 pA, scale bar = 9.1 Å). g. Corresponding nc-AFM image (Z-offset: 95 pm above STM set point: 5 mV, 50 pA. Scale bar = 9.1 Å). h. Corresponding chemical structure of an infinite Co-metallated polymer, **7**.

We next investigated the electronic structure of these nanostructures by means of point scanning tunneling spectroscopy (STS) and dI/dV mapping at selected bias voltages (cf. Figures 4, S21-23). To this end, we first characterized the planarized species **2,** which reveals a HOMO–LUMO gap of 1.7 eV, while the gap of a dimer and a trimer of **3** reduces to 1.5 eV and 1.1 eV, respectively (cf. Figures S21 and S22). Figure 4 displays representative dI/dV spectra acquired at the selected positions of a section of polymer **3**, revealing pronounced resonances at -0.65 eV and 0.45 eV. By mapping the spatial distribution of such resonances and comparing to free-standing DFT simulations (cf. Figures 4 and S23), we could infer a bandgap of 1.1 eV, while reinforcing our rationalization of the electronic structure of the dimeric and trimeric linear oligomers, since their maps are analogous to polymer **3**. Thus, the electronic bandgap of polymer **3** is already set at the trimer stage. Notably, the bandgap of the corresponding dI/dV maps reveal distinct spatial distributions of the valence and conduction band states, reflecting their

different contributions from the π-conjugated porphyrin units and the indenyl linkers. In particular, the valence band is delocalized over the rim of the porphyrin monomers and the C=C links, whereas the conduction band shows a pronounced contribution at the edges of the five-membered ring moieties. Altogether, the indenyl coupling exemplifies a synthetic procedure to engineer porphyrinoid materials exhibiting C=C bonds that provide a direct π-conjugated pathway between the porphyrin units.

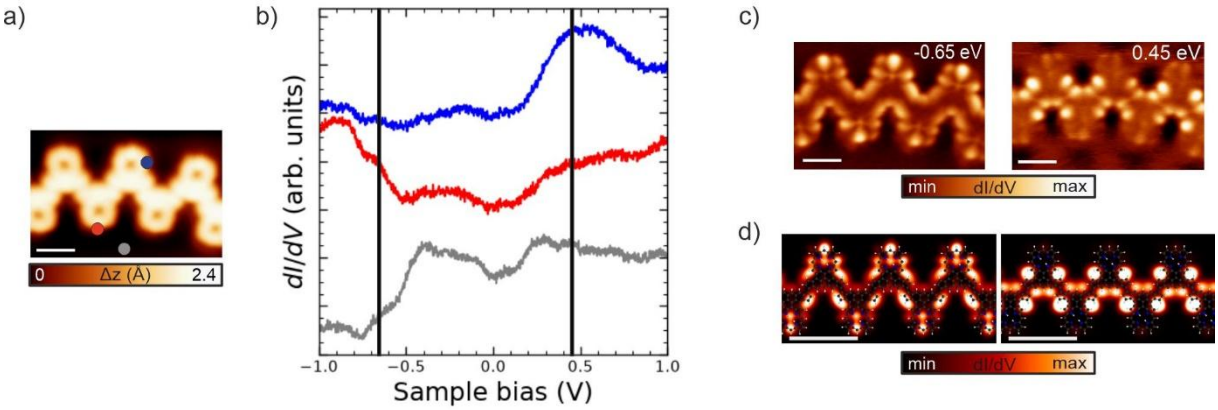


Figure 4 | Structural and electronic characterization of a section of polymer 3. a. Experimental constant-current STM image of a section of polymer **3** (V_b = 0.5 V, I_t = 50 pA, scale bar = 2.2 nm). b. Long range dI/dV spectra acquired on the positions indicated by colors in the STM image. Grey reference spectrum was taken on the Au(111) surface. Open feedback parameters for d*I*/d*V* spectra: V_b = -1.0 V, I_t = 200 pA, V_{rms} = 30 mV. c. Experimental dI/dV maps taken at the indicated energies (-0.65 eV and 0.45 eV). I_t = 250 pA. d. Corresponding simulated dI/dV maps, together with chemical schemes (scale bar = 2.2 nm).

Besides the dominant formation of 1D polymers, the reaction also yields a minor fraction (< 1%) of covalent cyclic porphyrin trimers, obtained as either the free-base species **4** or the Co-metallated analogue **8**. To the best of our knowledge, the formation of cyclic trimers **4** and **8** is unprecedented in on-surface synthesis.[32,38] The free-base cyclic trimer (**4**) adopts a highly symmetric triangular geometry (cf. Figures 5a-d) in which three porphyrin monomers are fused thanks to the homocoupling between carbons C1 and C9 of precursor **1** (cf. Figure 1). Notably, the precursor has lost all extra hydrogenation at their termini of the five-membered rings. As shown in Figure S24, high resolution STM and nc-AFM imaging of **8** reveal the same triangular framework as observed for **4**, with the three Co atoms appearing as characteristic bright protrusions at the centers of the porphyrin macrocycles in constant-height STM images. Altogether, the low yield of cyclic trimers suggests that their formation competes kinetically with further chain propagation and occurs only when three suitably oriented molecules meet on the surface.

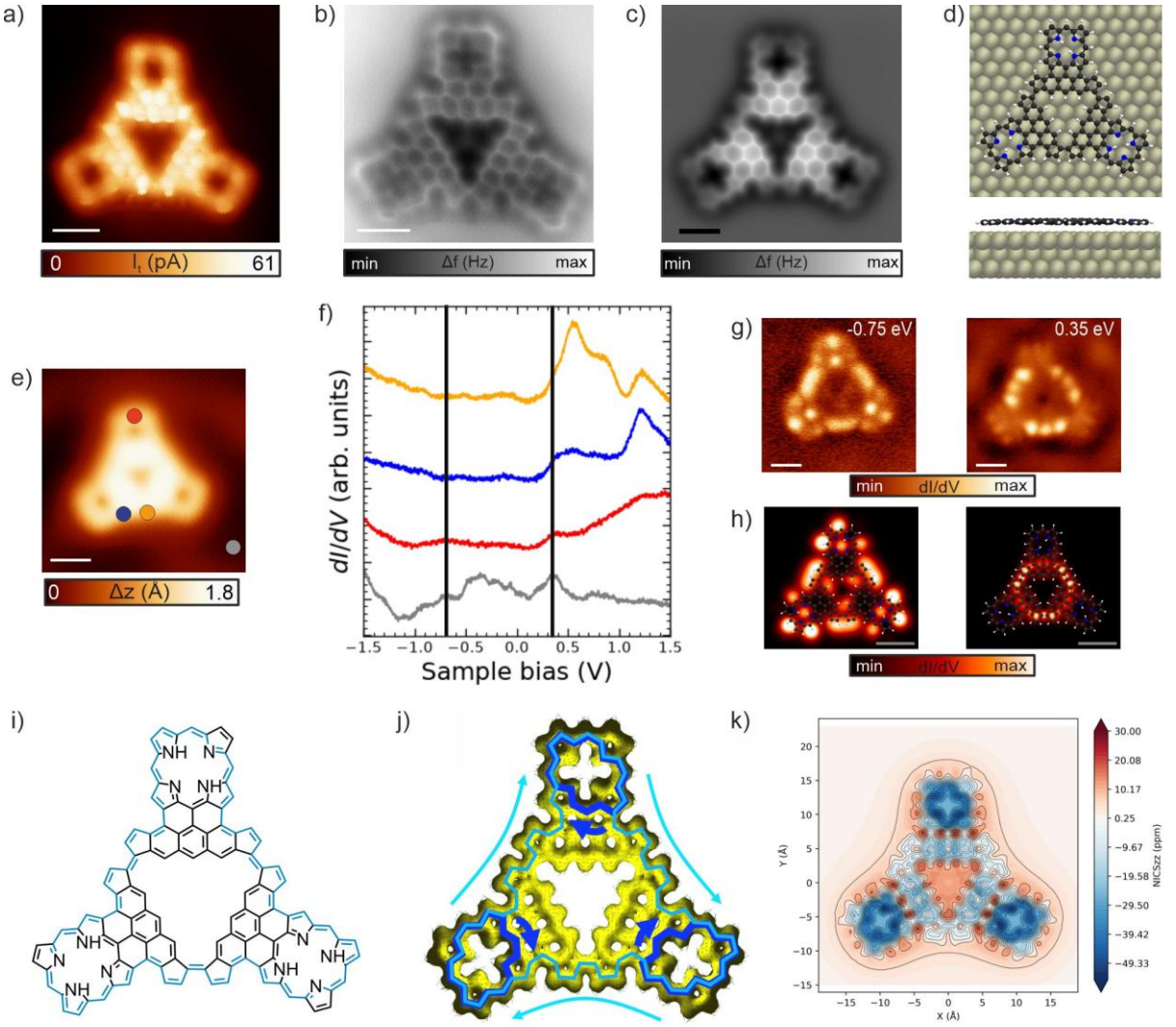


Figure 5. Structural, electronic and aromatic characterization of the cyclic free-base porphyrin trimer, 4. a. Constant-height STM image of trimer **4**. (V_b = 5 mV, I_t = 50 pA, scale bar = 6.6 Å). b, c. Experimental (Z-offset: 150 pm above STM set point: 5 mV, 50 pA. Scale bar = 6.2 Å) and corresponding simulated nc-AFM images (scale bar = 6.2 Å), respectively. d. Calculated adsorption geometry of trimer **4**. e. Constant-current STM image. (V_b = 50 mV, I_t = 250 pA, scale bar = 8.0 Å) f. dI/dV spectra acquired at the positions indicated by the colored dots in the previous STM image. A reference spectrum recorded on Au(111) is shown in grey. Open feedback parameters for d*I*/d*V* spectra: V_b = -1.5 V, I_t = 250 pA, V_{rms} = 30 mV. g. Experimental constant-current dI/dV maps recorded at the indicated bias voltages (-0.75 eV and 0.35 eV). I_t = 250 pA, scale bar = 8.0 Å. h. Corresponding simulated dI/dV maps. Scale bar = 1 nm. i. Representative resonance form of trimer **4**. j. AICD isosurfaces and current-density vectors illustrating the magnetically induced current distribution, with representative diatropic pathways indicated in blue. k. Spatially resolved NICSzz(1) map calculated at 1.0 Å above the molecular plane (blue: negative values; red: positive values). The cyclic trimer exhibits local macrocyclic aromaticity, together with a secondary global peripheral aromaticity.

Taking into account the potential interest in optoelectronics, we investigated the electronic properties of the free-base species **4**. To this end, we first performed STS at selected positions, as illustrated in Figures 5e and 5f. In the negative bias regime a dI/dV curve with increasing slope develops below -0.5 eV in comparison to the Au(111) reference signal, highlighting the presence of potential HOMOs; whereas in the positive bias regime a strong and broad resonance is observed, with a maximum at 0.55 eV. Mapping of the free-base cyclic trimer **4** at increasing bias steps of 100 meV, reveals the onsets of the HOMO at -0.75 eV, the LUMO at 0.35 eV and the LUMO +1 at 0.55 eV, which are in excellent agreement with the DFT-simulated ones, corroborating our rationalization, altogether highlighting a HOMO–LUMO gap of 1.1 eV (cf. Figures 5g, 5h and S25).

The aromatic character of the free-base cyclic trimer (cf. Figure 5i) was investigated using AICD calculations (cf. Figure 5j and Figure S26 for high resolution) in combination with NICSzz maps (Figure 5k). The current density distribution shows that π-electron delocalization cannot be described in terms of isolated aromatic rings, but instead arises from multiple coupled ring-current pathways extending across the entire conjugated framework. The most prominent feature of the AICD plot is the presence of a continuous diatropic current flowing along the outer perimeter of the molecule, demonstrating that the overall π-system sustains a global aromatic ring current involving 78 π electrons (cf. Figure S26). This suggests the presence of global aromaticity arising from long-range electron delocalization along the external boundary of the molecule. In addition to this global circuit, each of the three wing subunits (porphine moieties) supports its own independent diatropic macrocyclic current circulating around its perimeter and internal pore, demonstrating that each wing behaves as an aromatic macrocycle featuring the characteristic 18 π circuit. The system therefore exhibits aromatic circuits coexisting at multiple length scales: local macrocyclic and global. The NICSzz map of the cyclic trimer is fully consistent with the AICD results, showing strongly negative values in the wing subunits and along the outer perimeter.

To complement the qualitative AICD and NICSzz analysis, the magnetically induced current density was quantitatively evaluated, revealing three wing macrocycles as the preferential aromatic current pathways. Diatropic current strengths of 23.53, 24.00, and 24.41 nA/T were obtained for the three wings, respectively, corresponding to an average value of 23.98 $\pm$ 0.44 nA/T. Small opposite local contributions of only approximately 1.2 nA/T were detected within these integration regions, resulting in net currents of 22.23, 22.70, and 23.08 nA/T. The very small dispersion among the three symmetry-related wings, of only about 2%, provides an important internal consistency check for both the integration procedure and the assignment of these pathways. These results therefore confirm that the intense diatropic circulation observed around the wings in the AICD representation corresponds to a strong and essentially equivalent macrocyclic aromatic response in the three subunits. A diatropic current can also be identified along the external perimeter of the complete molecular framework. Integration through three symmetry-related sections of this outer pathway gives an average current strength of 10.62 $\pm$ 0.22 nA/T. However, its magnitude is markedly smaller than that obtained for the individual wing macrocycles. These quantitative results refine the aromaticity picture derived from the AICD and NICSzz analyses. The molecule displays aromatic circulation at different spatial scales, but these pathways are not equally favored. The dominant response corresponds to the three essentially equivalent aromatic wing macrocycles, which constitute the preferential current pathways of the π-conjugated framework. A weaker diatropic circulation nevertheless extends around the complete molecular perimeter, supporting the presence of a secondary global aromatic contribution.

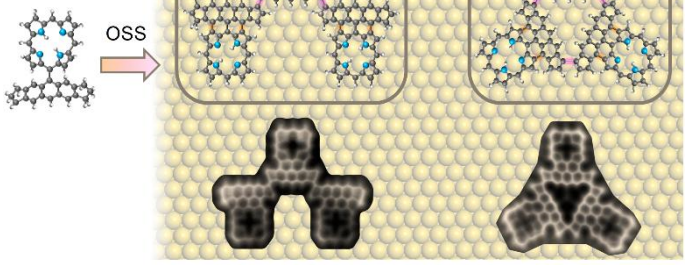
CONCLUSIONS

In summary, in this work we present a pioneering on-surface synthesis strategy that employs an indenyl coupling pathway to fabricate unique covalent porphyrin polymers. Taking advantage of an *ex-professo* synthesized free-base porphine monomer functionalized with a dicyclopentaanthracene moiety, to steer the coupling through the indene termini, it was possible to induce the regioselective formation of 1D staircase π-extended porphine-based polymers featuring a bandgap of 1.1 eV with high π delocalization. Notably, the reaction also yielded unique porphine-based cyclic trimers, displaying a HOMO–LUMO gap of 1.1 eV and a complex aromatic scenario yielding global peripheral aromaticity according to AICD and NICS calculations. Notably, the growth protocols also proved successful for Co-metallated precursors, yielding both linear polymers and cyclic trimeric species.

Our results introduce a novel strategy for harnessing the intrinsic properties of porphyrins within robust polymeric architectures. By demonstrating precise control over the synthesis of these electronically distinct linear and cyclic nanostructures, our findings pave the way for engineering bespoke organic nanomaterials with customized electronic landscapes. This work underscores the critical role of surface science in developing the next generation of functional molecular architectures for applications in optoelectronics, catalysis, and beyond.

More generally, our work demonstrates that indenyl coupling provides a versatile platform for engineering conjugated porphyrin nanoarchitectures, with programmable topology, electronic structure and aromaticity. Beyond porphyrins, this synthetic strategy opens new opportunities for constructing atomically precise molecular materials with tailored functionalities on surfaces.

TOC



Methods

STM and nc-AFM experiments

Molecular precursors **1** and **5** were deposited by thermal evaporation (Kentax TCE-BSC) with sublimation temperatures of 240 °C and 275 °C respectively, onto pre-cleaned Au(111) or Ag(111) surfaces. In order to promote the indenyl coupling and the dehydrogenative reaction between the macrocycle and the anthracene backbone, the samples were heated at the reported temperatures after the molecular deposition. These samples were previously prepared by several cycles of Ar+ ion sputtering (1.5 keV for 10 minutes) and subsequent post-annealing (450 °C for 10 minutes).

Experimental STM and nc-AFM experiments were performed in custom-designed UHV systems, with base pressures around 1·10-10 mbar, using a low-temperature Scienta Omicron microscope hosted at IMDEA Nanoscience for Au(111) substrates, and a LT-STM Createc, hosted at ICMM, for experiments on Ag(111).

For STM imaging and STS experiments, an electrochemically etched tungsten tip was employed. For nc-AFM imaging, a Qplus tuning fork sensor from Scienta Omicron, operating at 4.3 K, was used. This sensor was driven at its resonance frequency (around 26 kHz), with a constant oscillation amplitude of around 80 pm, controlled by a Zurich Instruments MFLI. Both of them, the tungsten tip and the Qplus tuning fork sensor, were functionalized with a single CO molecule (dosed at the surface for 10 seconds at $1{\cdot}10^{-8}$ mbar once the sample is prepared and cold). Scanning parameters are specified in each figure caption. dI/dV curves and maps were recorded using the lock-in technique (SR830 model).

Computational details

DFT Characterization:

For the geometry optimization of the molecules adsorbed on the Au(111) substrate, we used the FHI-AIMS Density functional theory package. [57] We employed different Au(111), 3-layered, orthogonal supercells for the adsorption on the isolated monomers, and trimers presented above. The lattice constant used for the Au(111) surface was $a = 4.0782$ Å, except for the case of the 1D infinite chains, which was $a = 4.3678$ Å, and that will be justified in the following paragraph. All these surfaces were designed to ensure a lateral separation of at least 1nm between the molecules and their periodic boundary conditions mirror images. The following dimensions for the supercells where used: Figure 2e (monomer) (10x10) with lattice vectors $\overrightarrow{a_1} = 28.837\text{Å}\,\hat{\imath}$ and $\overrightarrow{a_2} = 24.974\text{Å}\,\hat{\jmath}$, Figure 2k (trimer) (16x16) with lattice vectors $\overrightarrow{a_1} = 46.139\text{Å}\,\hat{\imath}$ and $\overrightarrow{a_2} = 39.958\text{Å}\,\hat{\jmath}$, Figure 4d (infinite 1D chains) (10x8) with lattice vectors $\overrightarrow{a_1} = 30.885\text{Å}\,\hat{\imath}$ and $\overrightarrow{a_2} = 21.398\text{Å}\,\hat{\jmath}$ and finally Figure 5d (cyclic trimer) (14x16) with lattice vectors $\overrightarrow{a_1} = 40.372\text{Å}\,\hat{\imath}$ and $\overrightarrow{a_2} = 39.958\text{Å}\,\hat{\jmath}$. Likewise, a perpendicular vector length of 3nm was used to ensure a sufficient layer of vacuum. The geometry optimizations were performed using the trust-radius-enhanced BFGS algorithm with a tolerance used for the convergence of the residual forces of $10^{-2}eV/\text{Å}$. The convergence parameters of each self-consistent step were set at $10^{-5}eV$ for the total energy, 10^{-4} Å^{-3} for the charge density and $10^{-2}eV$ for the sum of the Kohn-Sham eigenvalues. The atom-centered basis used where the tier 1 light basis functions provided with the FHI-AIMS package. The reciprocal space was described using the Γ-point of the first Brillouin zone and the optimizations were performed at the GGA-PBE level [58] with the Tkatchenko-Scheffler treatment of the van der Waals interactions.[58]

The characterization of the infinite chains was done first optimizing the gas phase lattice constant of the molecular chain, which was found to be 10.486 Å per molecule. Then a 10 x 8 supercell was built using a lattice constant of $a = 4.3678$ Å to match the lattice constant of the chains in the $[\overline{1}11]$ in which the molecular chains were experimentally found to align. The decision to apply the strain to the surface was taken after checking that using the regular lattice constant of $a = 4.0782$ Å for the surface and applying the subsequent strain to the molecular chains resulted on adsorption geometries that did not match the experimental results.

SPM simulations:

The AFM simulated images were obtained using the probe particle model,[59] with a k parameter for the stiffness of the CO terminated probe of $0.24\ N \cdot m^{-1}$ and a charge correction coefficient (q) of $-0.1\ e$ for the electrostatic interaction. The dI/dV simulated maps were also obtained using the probe particle model employing the eigenstates of the molecules, with their geometry optimized on the surface and in the absence of the substrate itself, calculated at the PBE0 hybrid potential, keeping their coordinates fixed in the ones obtained from the relaxation on the surface. The constant-current STM simulated image shown in Figure S11e was obtained with the probe particle model, obtaining first tridimensional matrix containing constant-current STM at different heights and then representing the Δz of constant-current isosurfaces within the STM data.

Aromaticity calculations:

The aromatic character of the free-base cyclic trimer was investigated by means of nucleus-independent chemical shift (NICS) calculations and anisotropy of the induced current density (AICD) analysis. All magnetic-response calculations were performed using Gaussian 16 (Revision C) at the B3LYP/def2-TZVP level of theory. To obtain spatially resolved NICSzz maps, the quasi-planar molecular structure was oriented with its average molecular plane coinciding with the XY plane (z = 0). A dense two-dimensional rectangular grid of ghost atoms (Bq) was subsequently generated at z = 1.0 Å, parallel to the molecular plane. The grid spacing was selected to achieve high spatial resolution while maintaining sufficient separation between neighbouring ghost atoms to avoid numerical instabilities. The lateral dimensions of the grid were extended to encompass the entire cyclic trimer and its surrounding region, allowing the magnetic response to be mapped across the complete conjugated framework. At each grid point, the out-of-plane component of the magnetic shielding tensor was extracted, with NICSzz defined as the negative of the corresponding σzz component. The resulting values were used to construct spatially resolved NICSzz(1) colour maps. The magnetically induced current density was further investigated using the AICD 3.0.4 program, employing magnetic-response data obtained from Gaussian calculations within the continuous set of gauge transformations (CSGT) formalism. The resulting current-density isosurfaces and vector fields were used to visualize the principal diatropic and paratropic current pathways within the conjugated molecular framework. To quantitatively characterize these pathways, the magnetically induced current-density tensor was reconstructed on the three-dimensional Cartesian grid employed for the AICD analysis (110 × 98 × 11 grid points). For an external magnetic field applied perpendicular to the molecular plane, the corresponding induced current-density vector field was obtained and integrated through cross-sectional surfaces-oriented perpendicular to the selected

conjugated pathways. Current strengths were evaluated from the flux of the induced current density through these surfaces and normalized to the applied magnetic field, yielding values in nA T^{-1}. Several slightly displaced equivalent integration planes were considered for each pathway to assess the sensitivity of the calculated current strengths to the precise location of the integration surface. The approximate threefold symmetry of the cyclic trimer provided an additional internal consistency check by allowing equivalent current pathways in the three porphyrinic subunits and along the external molecular perimeter to be independently evaluated. Further details of the numerical integration procedure and the resulting current strengths are provided in the Supplementary Information.

Acknowledgements

The authors thank Dr. Jorge Labella for fruitful discussions. We acknowledge to several funding organizations for their financial support. We thank funding from Spanish MCIN/AEI/10.13039/501100011033 through grants PID2019-108532GB-I00, PID2022-136961NB-I00, PID2022-140845OB-C62, PID2022-139933NB-I00, PID2024-155345NA-I00, PID2023-146373OB-I00, PID2025-168848NB-C21, PID2025-168848NB-C22, “María de Maeztu” Excellence Accreditation (CEX2025-001612-M) and “Severo Ochoa” Programme for Centers of Excellence in R&D (CEX2025001660-S). B.C. acknowledges support from RYC2024-049194-I. We appreciate funding from QUIMTRONIC-CM Y2018/NMT-4783, the ‘(MAD2D-CM)-IMDEA-Nanociencia’ and ‘(MAD2D-CM)-UCM’ projects funded by Comunidad de Madrid, by the Recovery, Transformation and Resilience Plan, and by NextGenerationEU from the European Union. The authors thank Comunidad de Madrid through Programa de Actividades de I+D (TEC-2024/TEC-459, SYNMOLMAT-CM). We appreciate funding from Xunta de Galicia (Centro de Investigación do Sistema Universitario de Galicia, 2023-2027, ED431G 2023/03). We thank support from the European Union (EU) through ERC SyG MolDAM (951519), while A.R.M. acknowledges the EU support under the MSCA-PF grant agreement no. 101150002 (GRAPHYRIN).

Data and Code Availability

The datasets generated during and/or analyzed during the current study are available from the corresponding author on reasonable request.

Author contributions

A. B., A.R.M., D. P. and D. E. conceived the project. A. R. M., J. B.-G., and D. P. synthesized the molecular compounds. A. G.-F., A. B., T. Q., A. M.-B., R. C., P. M., B. C. and D. E. acquired the experimental data, which was analyzed by A. G.-F., A. B., K. L., J. I. U., A. G., D. P., B. C. and D. E. J. I. M. and A. G. performed the calculations. A. G.-F., A. B., A. R. M., D. P. and D. E. wrote the manuscript with contributions from all the authors.

References

1. Senge, M.O., Sergeeva, N.N. & Hale, K.J. Classic highlights in porphyrin and porphyrinoid total synthesis and biosynthesis. *Chem. Soc. Rev.* **50**, 4730-4789 (2021).
2. Bonkovsky, H.L. *et al.* Porphyrin and Heme Metabolism and the Porphyrias. in *Comprehensive Physiology* 365-401 (2013).
3. Battersby, A.R. Tetrapyrroles: the pigments of life. *Nat. Prod. Rep.* **17**, 507-526 (2000).
4. Mauzerall, D. Porphyrins, Chlorophyll, and Photosynthesis. in *Photosynthesis I: Photosynthetic Electron Transport and Photophosphorylation* (eds. Trebst, A. & Avron, M.) 117-124 (Springer Berlin Heidelberg, Berlin, Heidelberg, 1977).
5. Mahmood, A. *et al.* Recent progress in porphyrin-based materials for organic solar cells. *J. Mater. Chem. A* **6**, 16769-16797 (2018).
6. Urbani, M., de la Torre, G., Nazeeruddin, M.K. & Torres, T. Phthalocyanines and porphyrinoid analogues as hole- and electron-transporting materials for perovskite solar cells. *Chem. Soc. Rev.* **48**, 2738-2766 (2019).
7. Paolesse, R., Nardis, S., Monti, D., Stefanelli, M. & Di Natale, C. Porphyrinoids for Chemical Sensor Applications. *Chem. Rev.* **117**, 2517-2583 (2017).
8. Meunier, B. Metalloporphyrins as versatile catalysts for oxidation reactions and oxidative DNA cleavage. *Chem. Rev.* **92**, 1411-1456 (1992).
9. Gu, S., Marianov, A.N., Lu, T. & Zhong, J. A review of the development of porphyrin-based catalysts for electrochemical CO2 reduction. *Chem. Eng. J.* **470**, 144249 (2023).
10. Xie, M., Liu, J., Dai, L., Peng, H. & Xie, Y. Advances and prospects of porphyrin derivatives in the energy field. *RSC Adv.* **13**, 24699-24730 (2023).
11. Day, N.U., Wamser, C.C. & Walter, M.G. Porphyrin polymers and organic frameworks. *Polym. Int.* **64**, 833-857 (2015).
12. Tian, J. & Zhang, W. Synthesis, self-assembly and applications of functional polymers based on porphyrins. *Prog. Polym. Sci.* **95**, 65-117 (2019).
13. Li, X.-G. *et al.* Porphyrin-based covalent organic frameworks from design, synthesis to biological applications. *Biomater. Sci.* **12**, 2766-2785 (2024).
14. Arshad, A. *et al.* Porphyrin-based covalent organic polymers and their composites: Advancing sustainable electrocatalysis for water splitting. *Renew. Sustain. Energy Rev.* **225**, 116120 (2026).
15. Shen, Q., Gao, H.-Y. & Fuchs, H. Frontiers of on-surface synthesis: From principles to applications. *Nano Today* **13**, 77-96 (2017).
16. Clair, S. & de Oteyza, D.G. Controlling a Chemical Coupling Reaction on a Surface: Tools and Strategies for On-Surface Synthesis. *Chem. Rev.* **119**, 4717-4776 (2019).
17. Wang, T. & Zhu, J. Confined on-surface organic synthesis: Strategies and mechanisms. *Surf. Sci. Rep.* **74**, 97-140 (2019).
18. Sun, Q., Zhang, R., Qiu, J., Liu, R. & Xu, W. On-Surface Synthesis of Carbon Nanostructures. *Adv. Mater.* **30**, 1705630 (2018).
19. Talirz, L., Ruffieux, P. & Fasel, R. On-Surface Synthesis of Atomically Precise Graphene Nanoribbons. *Adv. Mater.* **28**, 6222-6231 (2016).
20. Urgel, J.I. *et al.* On-Surface Covalent Synthesis of Carbon Nanomaterials by Harnessing Carbon gem-Polyhalides. *Adv. Mater.* **36**, 2402467 (2024).
21. Yang, B., Dong, B. & Chi, L. On-Surface Intramolecular Reactions. *ACS Nano* **14**, 6376-6382 (2020).
22. Zeng, W. & Wu, J. Open-Shell Graphene Fragments. *Chem* **7**, 358-386 (2021).

23. Pavliček, N. & Gross, L. Generation, manipulation and characterization of molecules by atomic force microscopy. *Nat. Rev. Chem.* **1**, 0005 (2017).
24. Björk, J., Hanke, F. & Stafström, S. Mechanisms of Halogen-Based Covalent Self-Assembly on Metal Surfaces. *J. Am. Chem. Soc.* **135**, 5768-5775 (2013).
25. Dong, L., Liu, P.N. & Lin, N. Surface-Activated Coupling Reactions Confined on a Surface. *Acc. Chem. Res.* **48**, 2765-2774 (2015).
26. Lackinger, M. Surface-assisted Ullmann coupling. *Chem. Commun.* **53**, 7872-7885 (2017).
27. Auwärter, W., Ecija, D., Klappenberger, F. & Barth, J.V. Porphyrins at interfaces. *Nat. Chem.* **7**, 105-120 (2015).
28. Gottfried, J.M. Surface chemistry of porphyrins and phthalocyanines. *Surf. Sci. Rep.* **70**, 259-379 (2015).
29. Diller, K. *et al.* In vacuo interfacial tetrapyrrole metallation. *Chem. Soc. Rev.* **45**, 1629-1656 (2016).
30. Di Santo, G. *et al.* Supramolecular Engineering through Temperature-Induced Chemical Modification of 2H-Tetraphenylporphyrin on Ag(111): Flat Phenyl Conformation and Possible Dehydrogenation Reactions. *Chem. Eur. J.* **17**, 14354-14359 (2011).
31. Papageorgiou, A.C. *et al.* Self-terminating protocol for an interfacial complexation reaction in vacuo by metal–organic chemical vapor deposition. *ACS Nano* **7**, 4520-4526 (2013).
32. Wiengarten, A. *et al.* Surface-assisted Dehydrogenative Homocoupling of Porphine Molecules. *J. Am. Chem. Soc.* **136**, 9346-9354 (2014).
33. Wiengarten, A. *et al.* Surface-Assisted Cyclodehydrogenation; Break the Symmetry, Enhance the Selectivity. *Chem. Eur. J.* **21**, 12285-12290 (2015).
34. Sun, Q. *et al.* Inducing Open-Shell Character in Porphyrins through Surface-Assisted Phenalenyl π-Extension. *J. Am. Chem. Soc.* **142**, 18109-18117 (2020).
35. Sun, Q. *et al.* Bottom-up Fabrication and Atomic-Scale Characterization of Triply Linked, Laterally π-Extended Porphyrin Nanotapes. *Angew. Chem. Int. Ed.* **60**, 16208-16214 (2021).
36. Tenorio, M. *et al.* Coordinative Self-assembly of π-Electron Magnetic Porphyrins. *Angew. Chem. Int. Ed.* **64**, e202420572 (2025).
37. Gu, Y. *et al.* A Poly(2,7-anthrylene) with peri-Fused Porphyrin Edges. *Angew. Chem. Int. Ed.* **64**, e202417129 (2025).
38. Rascon, E.C. *et al.* On-Surface Synthesis of Square-Type Porphyrin Tetramers with Central Antiaromatic Cyclooctatetraene Moiety. *J. Am. Chem. Soc.* **145**, 967-977 (2023).
39. Li, D. *et al.* Spin State in Au Porphyrins Modulated by Charge Transfer on Au(111). *J. Am. Chem. Soc.* **148**, 13863-13870 (2026).
40. Martínez García, M. *et al.* On-surface synthesis and interfacial charge redistribution of open-shell [3]triangulene-fused porphyrins on Au(111). *Natl. Sci. Rev.* **13**, nwag155 (2026).
41. Grill, L. *et al.* Nano-architectures by covalent assembly of molecular building blocks. *Nat. Nanotechnol.* **2**, 687-691 (2007).
42. Lafferentz, L. *et al.* Controlling on-surface polymerization by hierarchical and substrate-directed growth. *Nat. Chem.* **4**, 215-220 (2012).
43. Biswas, K. *et al.* Interplay between π-Conjugation and Exchange Magnetism in One-Dimensional Porphyrinoid Polymers. *J. Am. Chem. Soc.* **144**, 12725-12731 (2022).
44. Zhao, Y. *et al.* Quantum nanomagnets in on-surface metal-free porphyrin chains. *Nat. Chem.* **15**, 53-60 (2023).

45. He, Y. *et al.* Fusing tetrapyrroles to graphene edges by surface-assisted covalent coupling. *Nat. Chem.* **9**, 33 (2016).
46. Robles, R. *et al.* Tailoring π-d Magnetic Interactions in Metallated Porphyrin Nanotapes. *Angew. Chem. Int. Ed.* **64**, e15342 (2025).
47. Xiang, F. *et al.* Zigzag graphene nanoribbons with periodic porphyrin edge extensions. *Nat. Chem.* **17**, 1356-1363 (2025).
48. Chen, C. *et al.* Local Electronic Structure of a Single-Layer Porphyrin-Containing Covalent Organic Framework. *ACS Nano* **12**, 385-391 (2018).
49. Biswas, K. *et al.* Designing highly delocalized solitons by harnessing the structural parity of π-conjugated polymers. *Nat. Synth.* **4**, 233–242 (2025).
50. Biswas, K. *et al.* Driving Multi-Step Regioselectivity in On-Surface Polymer Synthesis by Molecular Coverage. *Angew. Chem. Int. Ed.* **64**, e202512575 (2025).
51. Rickhaus, M. *et al.* Global aromaticity at the nanoscale. *Nat. Chem.* **12**, 236-241 (2020).
52. Mishra, S. *et al.* Topological frustration induces unconventional magnetism in a nanographene. *Nat. Nanotechnol.* **15**, 22-28 (2020).
53. de Oteyza, D.G. & Frederiksen, T. Carbon-based nanostructures as a versatile platform for tunable π-magnetism. *J. Phys. Cond. Matter* **34**, 443001 (2022).
54. Liljeroth, P., Repp, J. & Meyer, G. Current-induced hydrogen tautomerization and conductance switching of naphthalocyanine molecules. *Science* **317**, 1203-1206 (2007).
55. Auwärter, W. *et al.* A surface-anchored molecular four-level conductance switch based on single proton transfer. *Nat. Nanotechnol.* **7**, 41-46 (2012).
56. Cirera, B. *et al.* On-Surface Synthesis of Gold Porphyrin Derivatives via a Cascade of Chemical Interactions: Planarization, Self-Metalation, and Intermolecular Coupling. *Chem. Mater.* **31**, 3248-3256 (2019).
57. Sun, Q. *et al.* Magnetic Interplay between π-Electrons of Open-Shell Porphyrins and d-Electrons of Their Central Transition Metal Ions. *Adv. Sci.* **9**, 2105906 (2022).
58. Tkatchenko, A. & Scheffler, M. Accurate Molecular Van Der Waals Interactions from Ground-State Electron Density and Free-Atom Reference Data. *Phys. Rev. Lett.* **102**, 073005 (2009).
59. Oinonen, N. *et al.* Advancing scanning probe microscopy simulations: A decade of development in probe-particle models. *Comput. Phys. Commun.* **305**, 109341 (2024).

Supplementary Files

This is a list of supplementary files associated with this preprint. Click to download.

- 2026NatureSynthesisPolymerizationofporphyrinsbyindenylcouplingSIvFinal.docx